PLOS BIOLOGY

Phe-Gly motifs drive fibrillization of TDP-43's prion-like domain condensates

David Pantoja-Uceda[1]☯, Cristiana Stuani[2]☯, Douglas V. Laurents[1], Ann E. McDermott[3], Emanuele Buratti[2], Miguel Mompeán[1,3]*

1 Rocasolano Institute of Physical Chemistry, Spanish National Research Council, Madrid, Spain,
2 International Centre for Genetic Engineering and Biotechnology, Trieste, Italy, 3 Department of Chemistry, Columbia University, New York, New York, United States of America

☯ These authors contributed equally to this work.
* mmompean@iqfr.csic.es

Abstract

Transactive response DNA-binding Protein of 43 kDa (TDP-43) assembles various aggregate forms, including biomolecular condensates or functional and pathological amyloids, with roles in disparate scenarios (e.g., muscle regeneration versus neurodegeneration). The link between condensates and fibrils remains unclear, just as the factors controlling conformational transitions within these aggregate species: Salt- or RNA-induced droplets may evolve into fibrils or remain in the droplet form, suggesting distinct end point species of different aggregation pathways. Using microscopy and NMR methods, we unexpectedly observed in vitro droplet formation in the absence of salts or RNAs and provided visual evidence for fibrillization at the droplet surface/solvent interface but not the droplet interior. Our NMR analyses unambiguously uncovered a distinct amyloid conformation in which Phe-Gly motifs are key elements of the reconstituted fibril form, suggesting a pivotal role for these residues in creating the fibril core. This contrasts the minor participation of Phe-Gly motifs in initiation of the droplet form. Our results point to an intrinsic (i.e., non-induced) aggregation pathway that may exist over a broad range of conditions and illustrate structural features that distinguishes between aggregate forms.

Introduction

Transactive response DNA-binding Protein of 43 kDa (TDP-43) is an RNA-binding protein that forms aberrant aggregates associated with disease contexts, including frontotemporal dementia (FTD) and amyotrophic lateral sclerosis (ALS) [1], or the recently reported "LATE" dementia, which had been misdiagnosed as Alzheimer disease [2]. TDP-43 also aggregates into functional amyloids [3] and participates in the assembly of various biomolecular condensates [4,5], which highlight the need for structural studies to understand the interplay between these aggregate forms. Structurally, TDP-43 contains a well-folded N-terminal [6] and 2 RNA-Recognition Motifs (RRM) domains [7] and a low-complexity, prion-like domain (PrLD) at its carboxyl terminus, which seems pivotal for the formation of the diverse amyloid and droplet forms. The TDP-43 PrLD is large (residues 267 to 414), comprising almost half the length of TDP-43, and is intrinsically disordered, with the exception of a short hydrophobic segment

Competing interests: The authors have declared that no competing interests exist.

Abbreviations: ALS, amyotrophic lateral sclerosis; BMRB, Biological Magnetic Resonance Bank; CPMAS, Cross-Polarization Magic Angle Spinning; DARR, Dipolar Assisted Rotational Resonance; FTD, frontotemporal dementia; GAroS, Gly, Aromatic, and Ser; LS, liquid-state; LSNMR, liquid-state NMR; NUS, non-uniform sampling; PrLD, prion-like domain; RRM, RNA-recognition motif; RT, room temperature; SS, solid-state; SSNMR, solid-state NMR; TDP-43, Transactive response DNA-binding Protein of 43 kDa; TEM, transmission electron microscopy; ThT, Thioflavin T.

(residues 318 to 340) that contains a helical region. This hydrophobic helix is followed by a Q/N-rich stretch (residues 341 to 367), and all this 318 to 367 (hydrophobic+Q/N) stretch is N- and C-terminally flanked by 2 segments rich in Gly, Aromatic, and Ser residues ("GAroS" segments, residues 273 to 317 and 368 to 414) [8]. Consensus exists that TDP-43 PrLD droplets or condensates can be induced with NaCl or RNA molecules and that structurally, droplet assembly is orchestrated by the hydrophobic helix [9–11], with moderate assistance of Trp and other aromatic residues within the 2 GAroS segments [11]. Importantly, this prior, seminal work did not detect maturation of the droplets into amyloid-like fibrils [9–12]. Conversely, Lim and colleagues reported that TDP-43 PrLD assembles amyloid fibrils, also driven by the hydrophobic helix, albeit they did not detect droplet formation [13]. These important observations suggest that droplet and fibril formation are end points of 2 distinct aggregation pathways, which intriguingly involve the same region within TDP-43 PrLD, namely the hydrophobic helix. However, this dichotomous picture (i.e., droplets or fibrils) contrasts with recent findings that proved that the droplet environment is conducive for fibril formation [14,15], as broadly established for other PrLD-containing proteins with GAroS regions [16–18].

Using polypeptide constructs corresponding to the TDP-43 PrLD central region (residues 311 to 360) that contains the critical helix, but excludes the 2 flanking GAroS segments (residues 267 to 310 and 361 to 414), the Eisenberg lab obtained cryo-electron microscopy (cryo-EM) structures of polymorphic fibrils with a common long β-hairpin named a "dagger-shaped" fold [19]. A most recent solid-state NMR (SSNMR) study on fibrils from this same 311 to 360 construct revealed key intermolecular contacts that are not compatible with the long β-hairpin structure seen by cryo-EM [15], which supports a distinct fibril conformation. Interestingly, these fibrils stem from droplets [15]. Although these constructs correspond to a limited part of the TDP-43 PrLD sequence as they exclude the 2 GAroS segments, these model fibrils already reveal the rich diversity of the TDP-43 PrLD amyloid foldome, which assembles distinct functional (e.g., in muscle regeneration) [3] and pathological (e.g., in FTD) [20,21] amyloid-like structures. However, we do not know if the structures formed by the TDP-43 PrLD (311 to 360) constructs recapitulate those adopted by the entire TDP-43 PrLD, which contains the 2 flanking GAroS regions (i.e., 267 to 310 and 361 to 414) that are relevant for droplet formation [11].

All the above observations pertinent to TDP-43 PrLD aggregation pathways have been carried out at pH values ranging from 6.0 to 8.0 and rely on droplet induction by salt or RNA molecules [9–12,14]. These efforts have lead to the successful elucidation by NMR of the helix-driven, GAroS-assisted mechanism of droplet assembly at the residue level [9–12]. However, we lack such fundamental knowledge on the intrinsic aggregation (i.e., in the absence of inducers) of TDP-43 PrLD at low pH. So far, only Lim and colleagues have reported an NMR characterization of the TDP-43 PrLD at pH 4, and they found no aggregation at all within months, even at protein concentrations as high as 600 μM [13]. This is in contrast with the observations we inform on this manuscript, where TDP-43 PrLD aggregates at pH 4, even when no salts or other aggregation inducers (e.g., RNAs) are present. Intense metabolic activity lowers pH, which induces stress granule formation [22–24] where TDP-43 is reported to form harmful ALS-relevant aggregates [5,25]. These aspects of TDP-43 aggregation in pro-pathological and pro-physiological contexts prompted us to structurally characterize the aggregation pathway of TDP-43 PrLD at pH 4 at the residue level, using liquid-state (LS) and solid-state (SS) NMR spectroscopies.

In the following, we report 3 fundamental aspects of TDP-43 PrLD, namely (i) that the full TDP-43 PrLD (residues 267 to 414) form droplets at pH 4 and in the absence of ions or RNA molecules; (ii) that these droplets do not represent end point species from this intrinsic aggregation pathway, but instead afford amyloid accumulation at the droplet surface/solvent

interface; and (iii) that such amyloid cores are stabilized by Phe residues from GAroS regions, located outside the central region containing the hydrophobic helix.

Results

The TDP-43 PrLD intrinsically self-aggregates at pH 4 to enable droplet formation

We observed that the PrLD of TDP-43 aggregated at pH 4 in the absence of salt or RNA, which, to the best of our knowledge, was unexpected [13,14]. Because induced aggregation at higher pH values is reported to be driven by the central region containing a helical segment [9,10], we sought to confirm whether this general mechanism is also operative under our conditions, using liquid-state NMR (LSNMR).

Considering that the TDP-43 PrLD is of low complexity (i.e., poor amino acid variability), aggregation prone, and chiefly disordered, the LSNMR ^{13}CO, $^{13}C\alpha$, $^{13}C\beta$, ^{15}N, ^{1}HN, $^{1}H\alpha$ and $^{1}H\beta$ correlations were obtained using a nonconventional strategy that affords robust and complete assignments with a minimal set of experiments. In brief, this approach is based on the unambiguous determination of sequential connectivities between all spin systems (except prolines) by direct correlation of the ^{1}HN and ^{15}N amide groups of one amino acid residue to those of the next residue in the sequence, followed by the assignment of each $^{13}C\alpha$ and $^{13}C\beta$ nuclei to corroborate the identity of the sequential fragments interrupted by prolines (see Methods and S1 and S2 Tables for a more detailed description). This methodology proves useful for low-complexity stretches and aggregation-prone samples and allowed us to assign all residues under the conditions of this study (Biological Magnetic Resonance Bank [BMRB] entry 50154) [26].

The ^{1}H-^{15}N HSQC spectrum of TDP-43 PrLD displayed poor chemical shift dispersion in the ^{1}HN dimension, consistent with a disordered domain (Fig 1A), and the NMR assignments confirmed the presence of the α-helix in the central region of TDP-43 PrLD (at residues 320 to 340) (Fig 1B). In addition to the helical region, Li and colleagues have shown that aromatic residues within the GAroS segments outside the central region are also relevant to some extent to the assembly process [11]. In order to interrogate the role of the helical component and the GAroS regions in the intrinsic aggregation of TDP-43 PrLD at pH 4, we analyzed peak intensities of the ^{1}H-^{15}N HSQC spectrum. This strategy has been used to characterize the helix-driven aggregation pathway of TDP-43 PrLD upon droplet induction with salt at higher pH values [10,11]. The peak intensities observed for the first ^{1}H-^{15}N HSQC spectra recorded within the first hour from sample preparation at 2 different concentrations (55 and 110 μM) revealed nonhomogeneous peak intensities throughout the PrLD sequence, with reduced intensity for the central residues containing the helical segment (Fig 1B, black bars), which is interpreted as shift from the monomeric toward the aggregate state mediated by helix–helix intermolecular interactions, in line with previous observations [9–12]. Over the course of approximately 20 hours, the greater signal intensity loss of the central region became more evident at both concentrations (Fig 1B, red bars). A closer inspection of these data revealed that, in addition to the central region containing the helix, other signals show reductions in signal intensity. Although these are minor changes, they are consistently observed over time and at the 2 concentrations (55 and 110 μM) as lower than average intensity values and mostly map to the 2 GAroS segments that are N-terminal (residues 267 to 310) and carboxyl terminus (361 to 414) to the central 311 to 360 region (Fig 1B, dashed horizontal lines). In particular, we highlight the following stretches of hydrophobic residues: 4 Phe-Gly-rich motifs at positions 276 to 284, 288 to 290, 367 to 368, and 396 to 403; 1 Tyr-Ser-Gly motif at 373 to 376; and 2 Trp-Gly motifs at positions 384 to 386 and 411 to 413 (Fig 1B and 1C). This result correlates very well with
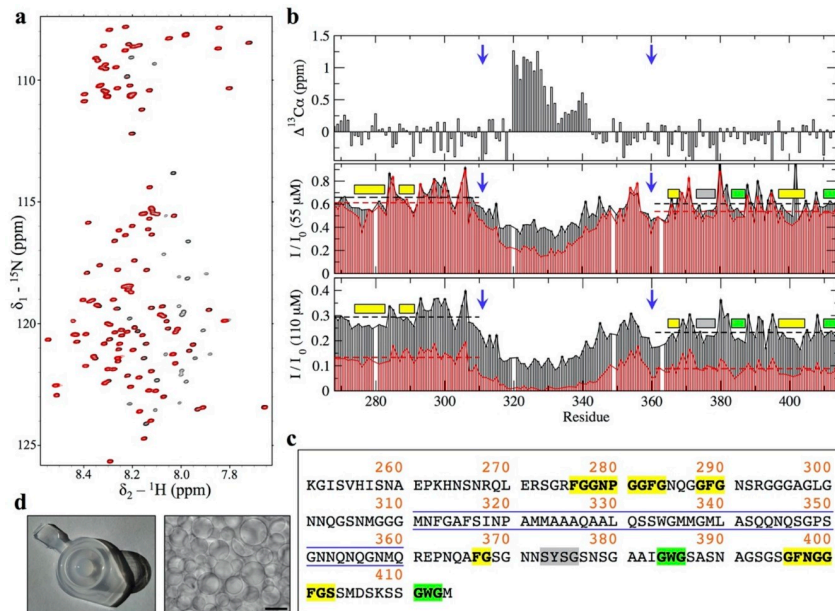
Fig 1. LSNMR characterization of the PrLD of TDP-43's aggregation at low pH. (a) The ^{1}H-^{15}N HSQC spectra of TDP-43 PrLD at pH 4 and 25°C (110 μM), showing a narrow ^{1}H amide chemical shift range typical of a disordered region. Black peaks correspond to a spectrum recorded within 1 hour from sample preparation, the time elapsed between column elution and the start of the NMR experiments (see Methods). The spectrum in red was the last recorded on this sample (S1 and S2 Tables), where signals corresponding to some but not all residues disappear due to self-association. **(b)** Signals whose intensity is lost over time correspond to the central region spanning residues 311–360 (delimited by blue arrows), which contain an α-helix as evinced by ^{13}Cα chemical shifts (top panel). In addition, several short segments within the 2 regions N-terminal and carboxyl terminus to the 311–360 core (i.e., 267–310 and 361–414) also exhibit moderate signal loss, which are consistently observed at 55 μM (middle panel) and at 110 μM (bottom panel). This is illustrated by plotting the intensity values from the first ^{1}H-^{15}N HSQC (I_0, black bars, 1 hour from sample preparation) and those from a ^{1}H-^{15}N HSQC recorded approximately 20 hours later, plotted as I/I_0 (red bars, I and I_0 correspond to intensity values for the second and first ^{1}H-^{15}N HSQC, respectively, normalized to the most intense peak). Note that average values for the 2 regions 267–310 and 361–414 N-terminal and carboxyl terminus to the central segment are shown as dashed horizontal lines (black and red colors for the I_0 and I/I_0 data sets, respectively), which highlights that the regions with lower than the average intensities mostly map to segments containing aromatic residues: Phe (yellow boxes), Tyr (gray box), and Trp (green boxes). **(c)** TDP-43's PrLD sequence illustrating the central region composed of residues 311–360 (blue lines, to match blue arrows in panel b), which was the focus of some earlier studies and contains the helical segment important for assembly, as well as the aromatic residues outside this core (Phe in yellow, Tyr in gray, and Trp in green). **(d)** At the end of the NMR experiments, the samples were found aggregated (left panel) and displayed extensive droplet formation (right panel, scale bar: 100 μm). This was imaged on the 110 μM sample. The ^{15}N-^{1}H HSQC spectra are available from Mendeley Data (http://dx.doi.org/10.17632/gyy4tc5nky.1), and the NMR chemical shifts are deposited in the BMRB under accession code 50154. Numerical data for the 3 plots in panel B can be found in S1 Data. BMRB, Biological Magnetic Resonance Bank; LSNMR, liquid-state NMR; PrLD, prion-like domain; TDP-43, Transactive response DNA-binding Protein of 43 kDa.

https://doi.org/10.1371/journal.pbio.3001198.g001

mutational analyses that showed that, in addition to the helical region, Phe283, Phe289 (in the GAroS segment that is N-terminal to the helix) and Tyr374, Trp385, Phe401, and Trp412 (in the GAroS carboxyl terminus to the helix) are required for droplet induction, since their mutation to glycines abolish salt-induced aggregation [11]. On this basis, we reasoned that the intrinsic aggregation we observed here does not follow an alternative mechanism with respect to that firmly established in the literature [9–12].

After approximately 7 (at 55 μM) or approximately 3.5 days (at 110 μM), the signals corresponding to residues within the central region and GAroS segments disappeared (Fig 1A, red spectrum), and we observed that the NMR samples contained aggregated material displaying extensive droplet formation (Fig 1D). Overall, these findings evince that (i) the TDP-43 PrLD self-assembles at low pH and without salt, conditions where it was reported to not aggregate

[13,14]; and that (ii) the aggregation process follows a helix-driven, GAroS-assisted mechanism of phase separation into droplets similar to that reported under droplet induction by salt or RNAs [9–12]. We interpret these observations as an intrinsic aggregation pathway of TDP-43 PrLD that is solely encoded by its amino acid sequence. Thus, it may well manifest over a broad range of conditions in cells, which would lead to the formation of relevant aggregate species at pH values below those normally considered physiological but relevant for metabolic stress conditions [5] and lysosome interiors [27]. Considering that all the prior work that uncovered the mechanism of droplet assembly did not detect fibrils (i.e., droplets were end point species following TDP-43 PrLD aggregation) [9–12], possibly since RNA and salt may hinder liquid to solid transitions, we next interrogated whether the droplets we detect could evolve into amyloid-like assemblies.

The TDP-43 PrLD droplet environment outbursts amyloid fibrils at the droplet surface/solvent interface

Following the discussion of droplet versus fibrils as end point of distinct aggregation pathways, it has been very recently proposed that droplet assembly in FUS, hnRNPA1, and potentially most archetypical PrLDs, is encoded by its primary sequence as enabled by a symmetric distribution of aromatic residues. More precisely, this refers to aromatic Phe, Trp, or Tyr "stickers" residues separated from each other by stretches of 3 to 12 "spacers" residues, such as Ser or Gly [28]. Within this framework, such symmetric distribution is not fulfilled if the aromatic stickers cluster together in the primary sequence (i.e., without interspaced residues), and this causes irreversible fibrillization instead over droplet formation [28]. We identified such a "sticker-and-spacers" symmetric distribution in the GAroS regions of TDP-43 PrLD, which may explain the intrinsic aggregation that we proposed to be encoded solely by its primary sequence. More precisely, the N-terminal region to the α-helix contains 3 Phe "sticker" residues, Phe276, Phe283, and Phe289, which are separated by 2 stretches of "spacers" spanning 6 (F_{276}GGPNGGF$_{283}$) and 5 (F_{283}GNQGGF$_{289}$) residues, respectively (Fig 1D). Similarly, the GAroS region that is carboxyl terminus to the α-helix contains 6 aromatic residues, which can be grouped in the following sticker-and-spacers pairs: Tyr374–Trp385 (separated by 10 spacers: Y_{374}SGSNSGAAIGW$_{385}$), Trp385–Phe397 (separated by 11 spacers: W_{385}GSAS-NAGSGSGF$_{397}$), Phe397–Phe401 (separated by 3 spacers: F_{397}NGGF$_{401}$), and Phe401–Trp412 (separated by 10 spacers: F_{401}GSSMDSKSSGW$_{412}$) (Fig 1D). Therefore, our interpretation that the lower peak intensities in the ^{1}H-^{15}N HSQC mapping to the GAroS regions resulted from intermolecular interactions driving the monomer to droplet transition (Fig 1B) fits well within this stickers-and-spacers model for PrLD-containing proteins and is in agreement with the conformational evolution revealed by Trp fluorescence, as the wavelength of maximum Trp emission, which is high during the first 10 hours (approximately 357 nm), red-shifts to approximately 350 nm after 1 day, indicating a transition from a high polar environment toward a somewhat less polar milieu (Fig 2A). In line with these observations, light scattering values were low at the beginning and sharply increased over the next several hours, approximately coinciding with the NMR signal loss (Fig 2A). During this period, the scattering remains steady for several hours and then increases further after 1 day, suggesting the formation of 2 distinct assembled species.

One distinctive feature between TDP-43 PrLD and other PrLDs is the helical region; its tendency to self-aggregate not only reduces the number of "stickers" required for droplet formation [11], but also drives the assembly of amyloid fibrils in distinct aggregation pathways [13,14]. Similar to the light scattering experiment, fluorescence anisotropy measurements suggested the formation of 2 distinct species, particularly, low anisotropy values characteristic of
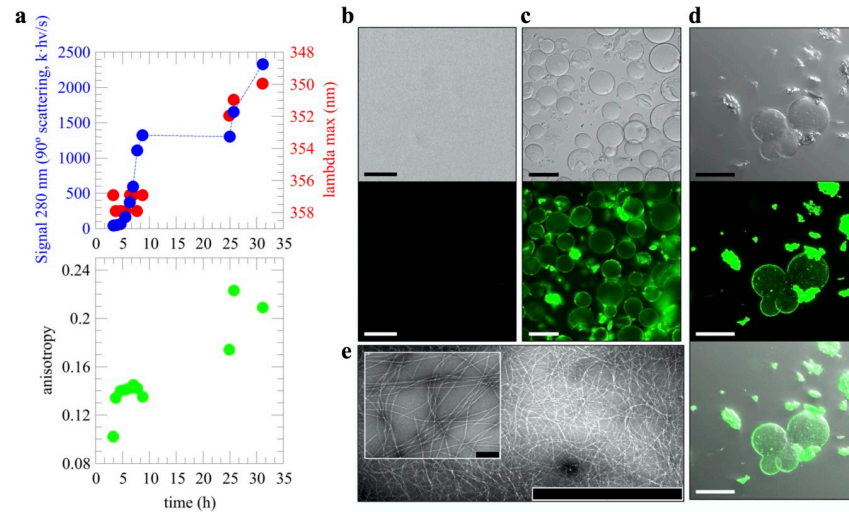
Fig 2. Droplet assembly is coupled to fibril formation. (a) Light scattering following the signal at 280 nm over time (top, blue circles), maximum emission wavelength (top, red circles), and fluorescence anisotropy (bottom, green circles) over time during droplet and fibril formation. **(b)** The TDP-43's PrLD sample eluted from the column is free of droplets (top). To test for the presence of amyloid fibrils, ThT was added to the sample and visualized by fluorescence microscopy (bottom). The lack of fluorescence indicates that no amyloid fibrils are present at the beginning of the experiments. **(c)** Aggregated samples (i.e., samples where no signal is detected in LSNMR experiments) present extensive droplet formation, as well as irregularly shaped clumps (top, light transmitted image). Interestingly, both the droplets and the clumps were recognized by ThT (bottom, fluorescent image). These images were collected using fluorescence microscopy on 110 μM TDP-43 PrLD. The scale bars in panels a and b are 100 μm. **(d)** Confocal microscopy images of the 55 μM aggregated sample (transmitted light, top; fluorescence, middle; overlay, bottom) showing ThT bound to droplets surface as well as to the irregularly shaped clamps, suggesting that the latter are made by amyloid fibrils which are formed and released from the droplet surface. Scale bar is 50 μm. **(e)** TEM micrographs confirmed the presence of amyloid fibrils, in agreement with ThT fluorescence (scale bar: 2 μm; at inset image: 200 nm). Numerical data for panel A can be found in S1 Data. PrLD, prion-like domain; TDP-43, Transactive response DNA-binding Protein of 43 kDa; TEM, transmission electron microscopy; ThT, Thioflavin T.

https://doi.org/10.1371/journal.pbio.3001198.g002

flexibility are observed that the earliest time point (approximately 0.10) and quickly increase to moderate values (approximately 0.14). After 1 day, higher values that are similar to those seen on Trp side chains in folded proteins or rigid complexes are measured (Fig 2A). Interestingly, Thioflavin T (ThT) fluorescence enhancement was only detected when the putative second species form, but not earlier, suggesting that amyloid formation occurred following droplet assembly. Direct visualization by confocal microscopy reveals a strong enhancement of ThT fluorescence in the droplets formed in the 2 samples at 55 and 110 μM (Fig 2B–2D) and, consistent with the data presented, dense networks of fibrils were imaged by transmission electron microscopy (TEM) (Fig 2E). The observation of ThT-reactive droplets in 2 distinct samples that aggregated following the same mechanism, as uncovered by LSNMR (Fig 1B), together with the imaging of the fibrils by TEM and the analysis of the conformational evolution, firmly establishes that TDP-43 PrLD fibril formation is coupled to droplets under these conditions.

The above results evoke the recent work by Gui and colleagues, who used ThT fluorescence and confocal microscopy to provide direct visual evidence that fibrils from hnRNPA1—another protein with a PrLD—formed from induced protein droplets [16]. A close inspection to both hnRNPA1 in Gui and colleagues' paper and TDP-43 PrLD in the present work revealed a critical difference: Whereas ThT fluorescence shines from the droplet interior in hnRNPA1 aggregates, indicative of fibrils confined within the droplet interior, the TDP-43 PrLD fibrils seems to be present at the surface, but not inside the droplet. One distinctive advantage of confocal microscopy is the possibility of scanning the entire volume of a droplet,
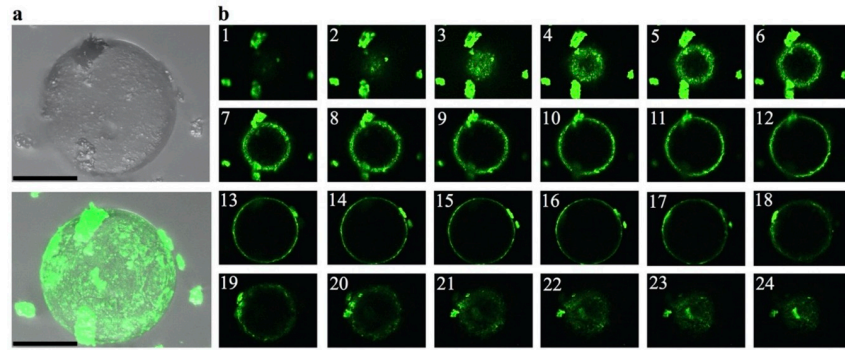
Fig 3. ThT-positive, TDP-43's PrLD fibrils emerge from protein droplets. (a) Visualization of a ThT-stained droplet from the 110 μM aggregated sample by confocal microscopy (top: transmitted light image, bottom: overlay with the ThT fluorescent image; scale bar: 50 μm). The nonhomogeneous staining suggests that fibril assembly occurs on droplet surface, and not its interior. Scale bar is 50 μm. **(b)** Sections of the droplet evince that the droplet interior is devoid of fibrils, whereas ThT fluorescence maps the droplet surface, at the droplet/solvent interface boundaries, and suggests detachment of fibrils once a certain size is reached. Images 1–24 are selected sections from a collection of 42 slices passing from pole to equator to pole that illustrate the distribution of ThT-positive aggregates across the droplet surface. PrLD, prion-like domain; TDP-43, Transactive response DNA-binding Protein of 43 kDa; ThT, Thioflavin T.

https://doi.org/10.1371/journal.pbio.3001198.g003

slice by slice, and this feature allowed us to look in closer detail at TDP-43 PrLD droplets. In Fig 3, we provide direct visualization that fibrils are in the surface and not in the interior of the droplet. Furthermore, they seem to detach upon reaching a critical size (Fig 3A and 3B).

The SSNMR signature of TDP-43 PrLD fibrils reveals an amyloid core that builds on aromatic stickers

We have shown that, at low pH, TDP-43 PrLD has an intrinsic ability to assemble droplets by virtue of its central region and the GAroS segments with aromatic stickers and spacers (Fig 1A–1C). We have then shown that this intrinsic aggregation pathway couples droplet formation with the accumulation of amyloid fibrils at the droplet surface/solvent interface. What structural factors drive the conversion of fibrils? During droplet assembly, Trp-Gly motifs are the most important residues in assisting the helical region [9,11]. In fibrils, previous cryo-EM and SSNMR studies with the TDP-43 PrLD (311 to 360) peptides proved that the helical region suffices to form amyloid fibrils [15,19]. However, these peptides lack the GAroS regions (residues 267 to 310 and 361 to 414) and do not inform on their participation in the fibrillar structures, as they do in droplets [9,11] (Fig 1D). Thus, we ought to explore whether the symmetrically distributed aromatic residues within the TDP-43 PrLD GAroS would form part of the fibril core, by taking advantage of their unique structural signature in the NMR spectra.

We analyzed the aggregated material that became invisible to LSNMR by means of SSNMR. Although full structure determination by SSNMR requires multiple samples with different labeling schemes and in large quantities [29], we could reconstitute a modest amount of the fibril conformation that formed at the droplet/solvent interface. Cross-Polarization Magic Angle Spinning (CPMAS)-based experiments are sensitive to molecular mobility, allowing us to scrutinize the presence of aromatic residues immobilized within the fibril core. Fig 4A shows a ^{13}C-^{13}C spectrum recorded under appropriate conditions to ensure detection of sequential residues (i.e., j and j+1) that remain static and rigid. No Trp residues could be detected in the characteristic region corresponding to aromatic ^{13}C nuclei (i.e., no indole side chains are observed). This result is curious because Trp residues are key to droplet formation by the TDP-43 PrLD [9,11], such that their mutation to Gly abolish droplet initiation [11].
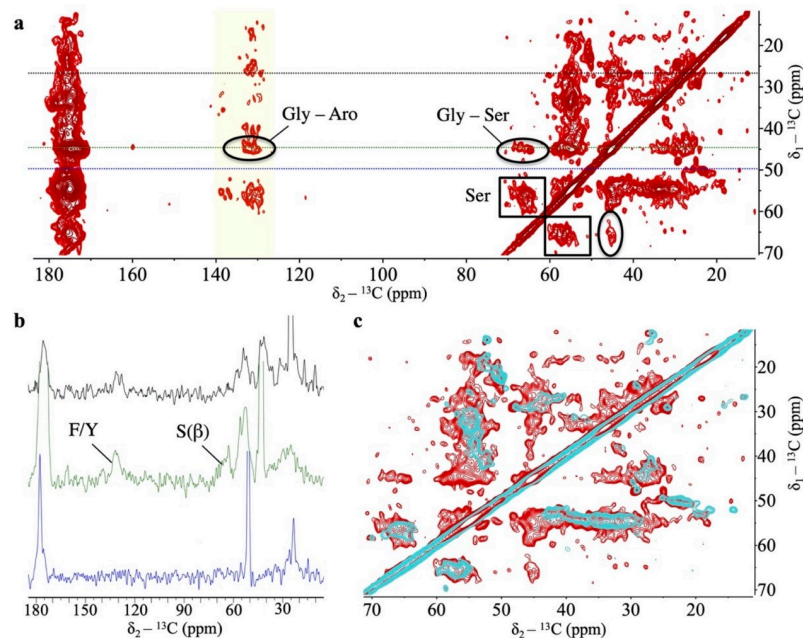
Fig 4. Fibrils from the PrLD of TDP-43 are stabilized by Phe-Gly motifs. (a) Two-dimensional ^{13}C-^{13}C DARR spectrum recorded with a 250 ms mixing time on fibrils formed by the PrLD of TDP-43. This experiment detects residues immobilized within the fibril core. Fibrils are rich in β-sheet content, as indicated by the presence of Ser residues showing differences of ^{13}Cβ-^{13}Cα > 8 ppm (black boxes). Cross-peaks between Ser and Gly (black ellipses) indicate that Ser-Gly motifs, which are located outside the helical region, are relevant in the fibril form. Signals around 130–140 ppm (yellow shaded region) correspond to aromatic ^{13}C from Phe/Tyr residues. Considering that there is only 1 Tyr in the PrLD sequence, most cross-peaks arise from Phe (^{13}Cδ/^{13}Cε)–Gly (^{13}Cα) (black circles). **(b)** Horizontal slices extracted from the 250 ms DARR shown in *a*, taken at δ$_1$ = 27.03 ppm (in black), which illustrates a crowded region that covers aliphatic, aromatic, and carbonyl peaks; δ$_1$ = 45.07 ppm (in green), which is distinctive of Gly ^{13}Cα chemical shift values, illustrating signals contributed by aromatic ^{13}C nuclei from Phe/Tyr, as well as by ^{13}Cβ of Ser, as identified by their distinctive chemical shift values. This supports the presence of immobilized Gly, Ser, and Phe residues in the fibril core; and δ$_1$ = 49.69 ppm (in blue), which lacks strong resonances thus facilitating an appreciation of the overall signal-to-noise of the SSNMR data. **(c)** A short mixing time (20 ms) 2D ^{13}C-^{13}C DARR spectrum (in cyan) overlapped onto the 250-ms spectrum from panel *a* (in red). At this short mixing, only intra-residue contacts are detected, which supports the assignment of sequential contacts that build up at larger mixing times. All these spectra are available from Mendeley Data (http://dx.doi.org/10.17632/gyy4tc5nky.1). DARR, Dipolar Assisted Rotational Resonance; PrLD, prion-like domain; SSNMR, solid-state NMR; TDP-43, Transactive response DNA-binding Protein of 43 kDa.

https://doi.org/10.1371/journal.pbio.3001198.g004

One potential explanation could be that Trp residues are exposed in the fibril, and not fixed in the core interior, such that their indole rings are on average less rigid and do not contribute strong signals in CPMAS-based experiments. However, the most striking observation is that we identified sequential contacts that correspond to several Phe/Tyr and Gly residues (Fig 4A), which unambiguously indicate that these motifs are immobilized within a fibrillar core containing β-rich segments, as evinced by distinctive cross-peaks in the Cα/Cβ serine region (Fig 4A). This is reminiscent of structural models of other PrLD-containing fibrils, in which the amyloid core is formed by Ser/Gly/Aromatic-rich motifs [30]. Unlike Trp residues, mutation of Phe residues to Gly did not abolish droplet initiation, as long as the Trp residues remained unchanged [11]. This observation indicates that Phe-Gly motifs have distinct roles in the droplet and the fibril forms. While a structure determination is still in progress, for which we are optimizing the production of larger amount of samples with distinct labeling schemes, the 1D slices of the 2D data set already indicate that the signal from Phe/Tyr aromatic ^{13}C, Gly's ^{13}Cα, and Ser's ^{13}Cβ nuclei are unambiguously detectable under our experimental conditions (Fig

4B). When the same experiment is recorded with a shorter mixing time, only intra-residual correlations are observed, supporting the build-up of sequential connectivities as the mixing time is increased (Fig 4C). The GAroS regions of TDP-43 PrLD contains 6 Phe-Gly motifs, 3 of which exist as Phe-Gly-Ser triads (Phe367, Phe397, and Phe401) (Fig 1C). There is also just 1 Tyr residue (Tyr374), which appears as Tyr-Ser-Gly (Fig 1C). Tentatively, it seems reasonable to speculate that these motifs may be part of the structural core. Along this line, a recent cryo-EM structural model of fibrils from the entire PrLD of TDP-43 formed under conditions akin to those of the present work was posted in bioRxiv [31] after the submission of this manuscript. Interestingly enough, this cryo-EM study provides direct visual evidence that all Phe residues from the GAroS segment are present in the structure, as proposed here based on the unambiguous observation of various cross-peaks corresponding to Phe residues in the aromatic region of the ^{13}C-^{13}C Dipolar Assisted Rotational Resonance (DARR) spectra (Fig 4). To further test the role of Phe residues within and outside the central region spanning residues 311 to 360, 2 TDP-43 PrLD variants were generated. In 1 variant, the 2 central Phe residues were substituted to Ala residues, that is F312A+F316A. In the other, all 6 Phe in the GAroS were mutated to Ala, that is F276A+F283A+F289A+F367A+F397A+F401A. When incubated in the presence of seeds from the SSNMR samples, the F313A+F316A variant formed aggregates, while the hexa-mutated F276A+F283A+F289A+F367A+F397A+F401A variant did not (S1 Fig). This result unambiguously indicates that whereas the double mutation can be tolerated and incorporates into the fibril, the hexa-mutated variant cannot. This observation corroborates the creation of hydrophobic cores by Phe residues in the GAroS segments, highlighting the relevance of these motifs beyond the central helix in forming amyloid fibrils by the PrLD of TDP-43.

Discussion

To date, several groups have presented studies of intrinsically disordered protein domains undergoing phase separation, wherein the microdroplets formed eventually evolve into amyloids [14–18]. Until now, it has been generally assumed that the residues responsible for forming the microdroplet are also those that become amyloid [13,15,32]. Here, we have combined LSNMR and SSNMR to obtain atomic level information on both processes. In contrast to previous expectations, we have uncovered that certain residues are responsible for droplet formation, whereas others are key for amyloidogenesis, including aromatic "sticker" residues proposed to enable reversible droplet formation and not fibrillization [28]. This discovery has important implications for our fundamental understanding of these processes. Excitingly, it means that we should be able to develop inhibitors or modulators that target the residues that are key for one process (i.e., the Phe residues which promote amyloidogenesis), without affecting the other residues which promote physiological droplet formation to confront the stress situation. This is also supported by the observation that TDP-43 PrLD also forms droplets that do not evolve into fibrils [9–12]. Importantly, these features could not be recruited in model fibrils from the 311 to 360 segments that exclude the GAroS segments harboring the Phe-Gly motifs (residues 267 to 310 and 361 to 414).

   We postulate that the fibril conformation that forms at pH 4 may represent a pro-pathological structure resulting from the persistence of a droplet state and that it may exist over a broad range of conditions based on the low content of titratable residues in the TPD-43 PrLD. This hypothesis is sustained by an intrinsic mechanism of droplet assembly, which remains essentially identical at pH 7 and in the presence of salts or RNA, and at pH4 without salts or RNA. Recently, Shenoy and colleagues carried out SSNMR measurements on TDP-43 PrLD fibrils assembled at pH 7.5 [33] and, interestingly, they did not report the Ser, Gly, and Phe/Tyr

signals that we detect under similar mixing time conditions in our 2D ^{13}C-^{13}C spectra from fibrils assembled at pH 4 (Fig 2A). This suggests the reconstitution of alternative structures in the 2 studies, which we explain based on the droplet stage reported, rather than different pH conditions. The droplet environment enabled fibrillization at the droplet surface/solvent interface, and such fibril form was amplified by seeding soluble protein, as this strategy is commonly used to propagate selected amyloid conformations [34–36]. Shenoy and colleagues used a 4-mm rotor in their SSNMR study, for which they successfully prepared a large amount of fibrillar material, but did not inform the formation of droplets [33]. This is reminiscent of the different outcomes observed in cryo-EM and SSNMR studies on fibrils from the TDP-43 PrLD (311 to 360) segment, in which the fibrils that form from droplets revealed spectral signatures not compatible with the cryo-EM structures [15,19]. These observations in aggregate support the view that TDP-43 PrLD participates in distinct aggregation pathways, with different end point species that include (i) droplets without fibrils [9–12,19]; (ii) fibrils without droplets [13,33]; and (iii) droplets and fibrils [14,15], as interpreted with the data informed to date. The droplet to fibril transitions are of potential relevance, as cytoplasmic TDP-43 droplets were shown to sequestrate components of the nuclear pore [37] and co-aggregate formation between TDP-43 and nuclear pore components emerged as a hallmark of ALS/FTD [38,39], and they may well be hybrid amyloids similar to the RIPK1-RIPK3 necrosome core [29]. Amid these diverse findings, ours are the first to directly link droplets to amyloid formation by combining LSNMR and SSNMR. Deciphering the structural features of the various TDP-43 aggregate species in diverse contexts [3,21], such as the Phe-Gly motifs shown here to create a fibril core, is an important step toward understanding physiological versus pathological aggregation.

Methods

Protein expression and purification

The N-terminally hexa-His-tagged PrLD construct corresponding to TDP-43(267–414) was a gift from Professor Nicolas Fawzi (Addgene plasmid # 98669). Proteins were overexpressed in *Escherichia coli* BL21 Star (DE3) (Life Technologies Carlsbad, California, United States of America). Uniform ^{15}N and ^{15}N/^{13}C labeling of TDP-43(267–414) was achieved by overexpression in M9 minimal media supplemented with ^{15}N ammonium chloride and ^{13}C glucose as the sole sources of nitrogen and carbon, respectively. *E. coli* BL21 Star (DE3) carrying TDP-43(267–414) were pre-inoculated overnight at 37°C. The day after, 200 ml of M9 minimal media were added to 4 mL of pre-inoculum, and the cell growth was monitored using Biophotometer D30 (Eppendorf, Hamburg, Germany) until the growth rate was 0.8 (OD at 600 nm). Then, the protein expression was induced overnight at 30°C by adding 1 mM IPTG.

Cells were collected by centrifugation at 7,000 × g for 1 hour 4°C, and the resulting pellet was resuspended in 30 mL lysis buffer (50 mM NaH$_2$PO$_4$, 300 mM NaCl, 10 mM Imidazole pH 8.0) supplemented with 1 tablet EDTA-free protease inhibitor cocktail (Roche Diagnostics Basel, Switzerland) and 1 mM PMSF (Sigma-Aldrich, St Louis, Missouri, USA). Cell lysis were performed using EmulsiFlex-C3 (Avestin Europe GmbH, Mannheim, Germany) and Bioruptor UCD-200 (Diagenode, Belgium). Inclusion bodies were recovered by centrifugation of cell lysate at 7,000 x g for 1 hour at 4°C and were resuspended in 20 mL denaturing binding buffer (20 mM Tris-Cl, 500 mM NaCl, 10 mM Imidazole, 1 mM DTT, 8 M urea, pH 8.0). Further centrifugation at 7,000 × g for 1 hour at 4°C was performed in order to pellet any remaining insoluble cell debris.

Ni-NTA Agarose beads (Qiagen, Gaithersburg, Maryland, USA) were used to bind the target protein and then were washed 3 times in 15 mL of denaturing binding buffer, and each

washing step was interspersed with centrifugation at $500 \times g$ for 5 minutes, room temperature (RT). Beads were then incubated with cell lysate for 4 hours rotating and successively collected by centrifugation at $500 \times g$ for 5 minutes, RT. Finally, beads were washed 3 times in 2 ml of denaturing binding buffer, and protein was eluted with imidazole gradient buffers, as described below:

1. 1 ml 20 mM Tris-Cl, 500 mM NaCl, 250 mM imidazole, 1 mM DTT, 8 M urea, with rotation of 2 hours at RT;

2. 1 ml, 20 mM Tris-Cl, 500 mM NaCl, 300 mM imidazole, 1 mM DTT, 8 M urea, with rotation overnight at 4°C;

3. 1 ml 20 mM Tris-Cl, 500 mM NaCl, 300 mM imidazole, 1 mM DTT, 8 M urea, with rotation of 2 hours at RT; and

4. 1 ml 20 mM Tris-Cl, 500 mM NaCl, 500 mM imidazole, 1 mM DTT, 8 M urea, with rotation of 6 hours at RT.

Each elution step was interspersed with centrifugation at $500 \times g$ for 5 minutes, RT, and from the total elution pool, approximately 3 mg of protein are obtained.

The pH of the samples from the TDP-43 PrLD constructs was then lowered to 4.0, and applied to a PD-10 gel filtration column (GE Healthcare, Little Chalfont, UK), which had been previously pre-equilibrated with the LSNMR buffer: 1 mM CD_3COOD in 85/15 H_2O/D_2O. The eluted fractions containing the PrLD construct, as identified by UV absorbance, were then concentrated to approximately 550 μL using an ultrafiltration device (Amicon, Danvers, Massachusetts, USA). The final urea concentration was less than 12 mM as determined by refractive index.

Choice of the best LSNMR assignment strategy

The TDP-43 PrLD is intrinsically disordered and low complexity (i.e., high redundancy in the amino acid sequence), and therefore poorly dispersed amide ^{1}H peaks and clustering of the ^{13}Cα and ^{13}Cβ chemical shifts around the random coil values are anticipated to complicate the assignment process. On the other hand, methods based on ^{13}C detection exploiting that ^{15}N and ^{13}CO signals remain well dispersed in disordered proteins cannot be applied to the TDP-43 PrLD, as these methods require high protein concentration conditions to overcome the low ^{13}CO sensitivity, under which TDP-43 PrLD quickly aggregates. With these limitations ahead, we resorted to ^{1}H-detected methods that mainly consist in connecting 2 consecutive NH groups through their correlations with 1 or more of the ^{13}C spins located between them: ^{13}Cα, ^{13}Cβ, and ^{13}CO. Due to the limitations mentioned earlier, we reasoned that six 3D experiments would be required to unambiguously obtain backbone chemical shifts, namely (i) HNCO; (ii) HN(CA)CO; (iii) HNCA; (iv) HN(CO)CA; (v) CBCA(CO)NH; and (vi) HNCACB. Recording this set of experiments with an acceptable resolution entails an average time of approximately 90 hours, as illustrated in S1 Table, which is by far too long for the TDP-43 PrLD to remain in solution due to its high aggregation tendency.

We then reasoned what would be the best strategy to accomplish the NMR assignments of our protein, ruling out the use of non-uniform sampling (NUS) schemes as the low concentration conditions the percentage of sampling that would be reduced may not represent a great time gain. With all these drawbacks, we proposed using a different strategy in which just three 3D experiments enabled unambiguous assignments of all signals in the ^{1}H-^{15}N HSQC spectrum of TDP-43 PrLD (S2 Table). The approach consists of 2 experiments, 1 H(NCOCA)HN and 1 (H)N(COCA)NH, that allowed us to directly connect consecutive amide groups from all

signals in the ^{1}H-^{15}N HSQC. Using the information from a CBCA(CO)NH experiment, the spin systems are well defined through the ^{13}Cα and ^{13}Cβ chemical shifts. With this strategy, experiments are acquired in a time of approximately 55 hours, that is to say, 37.5% less than the conventional triple resonance strategy described above. These experiments were recorded on the 110 μM sample, along with an additional HNCA to corroborate the assignments and to obtain the ^{13}CA chemical shifts for the 4 residues preceding prolines (P280, P320, P349, and P363) and for the last residue M414. The experiment time of the HNCA was 5.5 hours (S2 Table), which still represent a reduction of 31% with respect to the conventional approach listed in S1 Table. Finally, a CC(CO)NH experiment was recorded on this sample (experiment time 22.5 hours) to assign side chain ^{13}C nuclei from Gln, Arg, Lys, Pro, Ile, and Leu residues. After these approximately 3.5 days of NMR measurements, some signals in the ^{1}H-^{15}N HSQC are missing, and the sample was aggregated. To report the full set of backbone assignments, the ^{13}CO and ^{1}Hα chemical shifts were obtained by recording a HNCO (5.5 hours) and a HBHA(CO)NH (33.2 hours) on the 55 μM sample. The latter experiment also provides the assignments for ^{1}Hβ nuclei.

LSNMR experiments

The above LSNMR experiments were collected at pH 4.0 and 298 K on a Bruker AV-800 US2 (800 MHz ^{1}H frequency) spectrometer equipped with a cryoprobe and Z-gradients. The 2 samples (55 and 110 μM) were prepared by concentration of the eluted fractions to approximately 550 μL, from which 300 μL of were transferred into D$_2$O-matched, 5 mm Shigemi tubes. To obtain the ^{13}CO, ^{13}Cα, ^{13}Cβ, ^{15}N, ^{1}HN, ^{1}Hα, and ^{1}Hβ NMR assignments following the strategy presented in the previous section, we started from a root ^{1}H-^{15}N HSQC spectrum, which served as the first spectrum to carry out the peak intensity analyses in Fig 1. This experiment was measured again after approximately 20 hours with the following parameters: 4 scans, 12 and 20 ppm as spectral widths for ^{1}H and ^{15}N, respectively, and transmitter frequency offsets of 4.75 and 116.5 ppm for ^{1}H and ^{15}N, respectively. The remaining experiments to obtain chemical shifts to be deposited in the BMRB were recorded with the following parameters (see also S1 and S2 Tables):

CBCA(CO)NH (8 scans, 12, 20, and 75 ppm as ^{1}H, ^{15}N, and ^{13}C spectral widths, respectively, and transmitter frequency offsets of 4.75, 116.5, and 44 ppm for ^{1}H, ^{15}N, and ^{13}C, respectively); H(NCOCA)HN (12 scans, 12, 20, and 4.25 ppm as ^{1}H, ^{15}N, and ^{1}H spectral widths, respectively, and transmitter frequency offsets of 4.75, 116.5, and 7.125 ppm for ^{1}H, ^{15}N, and ^{1}H, respectively); (H)N(COCA)NH (12 scans, 12, 20, and 20 ppm as ^{1}H, ^{15}N, and ^{1}H spectral widths, respectively, and transmitter frequency offsets of 4.75, 116.5, and 116.5 ppm for ^{1}H, ^{15}N, and ^{15}N, respectively); HNCA (4 scans, 12, 20, and 30 ppm as ^{1}H, ^{15}N, and ^{13}C spectral widths, respectively, and transmitter frequency offsets of 4.75, 116.5, and 54 ppm for ^{1}H, ^{15}N, and ^{13}C, respectively); HNCO (8 scans, 12, 20, and 12 ppm as ^{1}H, ^{15}N, and ^{13}C spectral widths, respectively, and transmitter frequency offsets of 4.75, 116.5, and 174 ppm for ^{1}H, ^{15}N, and ^{13}C, respectively); HBHA(CO)NH (12 scans, 12, 20, and 6, ppm as ^{1}H, ^{15}N, and ^{1}H spectral widths, respectively, and transmitter frequency offsets of 4.75, 116.5, and 4.75 ppm for ^{1}H, ^{15}N, and ^{1}H, respectively), and a CC(CO)NH experiment (8 scans, 12, 20, and 75 ppm as ^{1}H, ^{15}N, and ^{13}C spectral widths, respectively, and transmitter frequency offsets of 4.75, 116.5, and 39 ppm for ^{1}H, ^{15}N, and ^{13}C, respectively).

Proton chemical shifts were directly referenced using DSS on a TDP-43 PrLD sample prepared for this purpose, and ^{13}C and ^{15}N chemical shifts chemical shifts were referenced indirectly. Conformational chemical shifts, Δ(^{13}Cα), where calculated as δ^{13}Cα(exp)—δ^{13}Cα(ref), with δ^{13}Cα(exp) being our measured chemical shifts and δ^{13}Cα(ref) reference values obtained

using the sequence of the TDP-43 PrLD construct and the data compiled by Poulsen, Dyson, and colleagues, at 25˚C and pH 4, as implemented in the chemical shift calculator (http://spin.niddk.nih.gov/bax/nmrserver/Poulsen_rc_CS) [40–42].

All spectra were processed using either NMRPipe [43] or Topspin 4.0.8 (Bruker Biospin, Germany), and peak-picking and spectral assignment was conducted using NMRFAM-Sparky [44]. The NMR chemical shifts are deposited in the BMRB under accession code 50154.

SSNMR experiments

SSNMR experiments were recorded on the aggregated material that formed following droplet formation during our LSNMR studies, which was amplified by seeding soluble protein prepared as described above. As a reference, from the most concentrated LSNMR samples (110 μM), the 300 μL from the Shigemi tube contains approximately 600 μg of material, assuming that 100% of the protein converted into fibrils when no signal is detected. After 3 weeks of incubation, the supernatant was carefully separated from the aggregated material settled on the bottom of the Eppendorf, which was lyophilized and transferred into a rotor using Bruker MAS rotor tools. The experiments were conducted on a Bruker 17.6 T spectrometer (750 MHz ^{1}H frequency) using an HCN 1.3 mm MAS probe. Moreover, 2D ^{13}C-^{13}C DARR spectrum [45] were recorded with mixing times of 20 and 250 ms, spinning the rotor containing the sample at a MAS rate of 17 and 20 kHz, respectively. The longer, 250-ms mixing time seemed appropriate to observe cross-peaks corresponding to sequential (j to j+1) residues, to detect correlations between Gly and Phe, Trp or Tyr, based on the characteristic chemical shifts of the Gly ^{13}Cα and ^{13}Caro chemical shift values distinctive for each type of aromatic residue. The spectra were recorded with the acquisition parameters listed in S3 Table, 64 scans, using a spectral width of 220.9 ppm in the direct and indirect dimensions, with acquisition times of 20 and 2.5 ms, respectively, and setting the transmitter frequency offset to 100 ppm. The DARR spectrum was processed using Topspin 4.0.8, with chemical shifts referenced to DSS.

Visualization of amyloid fibrils and protein droplets

Liquid droplets were directly visualized by spotting aliquots of the 2 (55 and 110 μM) samples onto glass coverslips using a Leica TCS SP2 inverted confocal microscope (Wetzlar, Germany) equipped with 7 laser lines, by both transmitted light (Fig 1D) and fluorescence imaging (Fig 2B). The latter were obtained by addition of 1 μL of 1mM ThT and laser excitation at 457 nm, following the protocol by Gui and colleagues [16]. To confirm that the ThT-reactive species were amyloids, the samples were directly adsorbed onto carbon-coated 300-mesh copper grids and negatively stained by incubation with 2% uranyl-acetate for direct visualization by TEM on a JEOL JEM-1011 electron microscope equipped with a TVIPS TemCam CMOS. Images acquired at a magnification of 30,000x and an accelerating voltage of 1,000 kV.

Fluorescence measurements

Fluorescence measurements were performed using a photon-counting Jobin–Yvon Fluoro-max-4 spectrofluorimeter equipped with emission and excitation polarizers and a Peltier temperature control device. Fluorescence spectra of TDP-43 PrLD were measured at 25˚C using a 280-nm excitation wavelength and recording emission from 270 nm to 400 nm with a scan speed of one half second per nm and excitation and emission slit widths of 2 nm. Using this approach, the 90˚ light scattering can be obtained as the apparent emission at 280 nm, while the Trp maximum emission wavelength and intensity provides information on how polar the indole fluorophore's environment is. Steady state anisotropy (A), measured at the wavelength

of maximal emission, was calculated as

$$A = (VV - VH)/(VV + 2 \cdot VH),$$

where VV is the steady state emission where both the excitation and emission polarizers are set to vertical (0˚), but the emission polarizer is set to horizontal (90˚). Values of anisotropy typically range from <0.10 for mobile protein Trp indole groups in statistical coils to >0.20 for Trp fixed in the rigid core of a folded protein [46].

Cross-seeding experiments

The wild-type TDP-43 PrLD (residues 267 to 414), as well as the 2 mutant variants were desalted from the 8 M urea-containing solution as explained above using a PD-10 column. A total of 5 μM of each protein variant in 1 mM CD_3COOD (NMR buffer) with 40 μM ThT was assayed for their ability to cross-seed with the fibrillar aggregates studied by SSNMR, by adding 2% of seeds to the reaction (0.12 μM). The seeding reactions were measured at 25˚C with excitation and emission wavelengths of 450 nm and 480 nm, respectively.

Supporting information

S1 Fig. Cross-seeding experiments. Cross-seeding in the polymerization into amyloid fibrils of the WT with respect to a double mutant, F313A+F316A, and a hexa-mutated construct, F276A+F283A+F289A+F367A+F397A+F401A, was studied by ThT binding assays. The distinct columns represent the following samples: column 1 is a blank, consisting of ThT (40 μM) in 1 mM CD_3COOD (blank), and columns 2 and 3 are 2 independent samples consisting of 2% (0.12 μM) of seeds (amyloid fibrils packed in the SSNMR rotor). The next 3 columns (4, 5, and 6) correspond to 3 independent samples from the WT TDP-43 PrLD (1 without and 2 with 2% seeds). In columns 7, 8, and 9, the results for the hexa-mutant (F276A+F283A+F289A +F367A+F397A+F401A, denoted as 6F > A) are presented (1 without and 2 with 2% seeds). Finally, columns 10, 11, and 12 correspond to the double mutant F313A+F316A (1 without and 2 with 2% seeds). ThT is at 40 μM in all instances, and the final protein concentration is always 6 μM. Seeds from the WT cannot induce amyloid formation in the 6F > A mutant protein, as revealed by the negligible ThT enhancement (*p*-values between "a" and "b" or between "b" and "c" <0.0001). In contrast, F313A+F316A is efficiently cross-seeded in the presence of 2% of seeds (*p*-value between "a" and "c" of 0.8224). Each independent sample is measured 5 times, and the corresponding numerical data can be found in S1 Data. PrLD, prion-like domain; TDP-43, Transactive response DNA-binding Protein of 43 kDa; ThT, Thioflavin T; WT, wild-type.
(TIFF)

S1 Table. Typical experiments for the unambiguous assignment of low-complexity, disordered proteins.
(XLSX)

S2 Table. Experiments used for the assignment of the TDP-43 PrLD. PrLD, prion-like domain; TDP-43, Transactive response DNA-binding Protein of 43 kDa.
(XLSX)

S3 Table. Acquisition and processing parameters used in the SSNMR experiments presented in Fig 4. SSNMR, solid-state NMR.
(XLSX)

S1 Data. Numerical data for Figs 1, 2 and S1.
(XLSX)

Author Contributions

References

1. Neumann M, Sampathu DM, Kwong LK, Truax AC, Micsenyi MC, Chou TT, et al. Ubiquitinated TDP-43 in frontotemporal lobar degeneration and amyotrophic lateral sclerosis. Science. 2006; 314:130–133. https://doi.org/10.1126/science.1134108 PMID: 17023659

2. Nelson PT, Dickson DW, Trojanowski JQ, Jack CR, Boyle PA, Arfanakis K, et al. Limbic-predominant age-related TDP-43 encephalopathy (LATE): consensus working group report. Brain. 2019; 142:1503–1527. https://doi.org/10.1093/brain/awz099 PMID: 31039256

3. Vogler TO, Wheeler JR, Nguyen ED, Hughes MP, Britson KA, Lester E, et al. TDP-43 and RNA form amyloid-like myo-granules in regenerating muscle. Nature. 2018; 563:508–513. https://doi.org/10.1038/s41586-018-0665-2 PMID: 30464263

4. Chu JF, Majumder P, Chatterjee B, Huang SL, Shen CJ. TDP-43 Regulates Coupled Dendritic mRNA Transport-Translation Processes in Co-operation with FMRP and Staufen1. Cell Rep. 2019; 29:3118–3133 e3116. https://doi.org/10.1016/j.celrep.2019.10.061 PMID: 31801077

5. Zhang P, Fan B, Yang P, Temirov J, Messing J, Kim HJ, et al. Chronic optogenetic induction of stress granules is cytotoxic and reveals the evolution of ALS-FTD pathology. Elife. 2019; 8. https://doi.org/10.7554/eLife.39578 PMID: 30893049

6. Mompeán M, Romano V, Pantoja-Uceda D, Stuani C, Baralle FE, Buratti E, et al. The TDP-43 N-terminal domain structure at high resolution. FEBS J. 2016; 283:1242–1260. https://doi.org/10.1111/febs.13651 PMID: 26756435

7. Lukavsky PJ, Daujotyte D, Tollervey JR, Ule J, Stuani C, Buratti E, et al. Molecular basis of UG-rich RNA recognition by the human splicing factor TDP-43. Nat Struct Mol Biol. 2013; 20:1443–1449. https://doi.org/10.1038/nsmb.2698 PMID: 24240615

8. Mompeán M, Baralle M, Buratti E, Laurents DV. An Amyloid-Like Pathological Conformation of TDP-43 Is Stabilized by Hypercooperative Hydrogen Bonds. Front Mol Neurosci. 2016; 9:125. https://doi.org/10.3389/fnmol.2016.00125 PMID: 27909398

9. Conicella AE, Zerze GH, Mittal J, Fawzi NL. ALS Mutations Disrupt Phase Separation Mediated by alpha-Helical Structure in the TDP-43 Low-Complexity C-Terminal Domain. Structure. 2016; 24:1537–1549 https://doi.org/10.1016/j.str.2016.07.007 PMID: 27545621

10. Li HR, Chen TC, Hsiao CL, Shi L, Chou CY, Huang JR. The physical forces mediating self-association and phase-separation in the C-terminal domain of TDP-43. Biochim Biophys Acta Proteins Proteom. 2018; 1866:214–223. https://doi.org/10.1016/j.bbapap.2017.10.001 PMID: 28988034

11. Li HR, Chiang WC, Chou PC, Wang WJ, Huang JR. TAR DNA-binding protein 43 (TDP-43) liquid-liquid phase separation is mediated by just a few aromatic residues. J Biol Chem. 2018; 293:6090–6098. https://doi.org/10.1074/jbc.AC117.001037 PMID: 29511089

12. Conicella AE, Dignon GL, Zerze GH, Schmidt HB, D'Ordine AM, Kim YC, et al. TDP-43 alpha-helical structure tunes liquid-liquid phase separation and function. Proc Natl Acad Sci U S A. 2020; 117:5883–5894. https://doi.org/10.1073/pnas.1912055117 PMID: 32132204

13. Lim L, Wei Y, Lu Y, Song J. ALS-Causing Mutations Significantly Perturb the Self-Assembly and Inter-action with Nucleic Acid of the Intrinsically Disordered Prion-Like Domain of TDP-43. PLoS Biol. 2016; 14:e1002338. https://doi.org/10.1371/journal.pbio.1002338 PMID: 26735904

14. Babinchak WM, Haider R, Dumm BK, Sarkar P, Surewicz K, Choi JK, et al. The role of liquid-liquid phase separation in aggregation of the TDP-43 low-complexity domain. J Biol Chem. 2019; 294:6306–6317. https://doi.org/10.1074/jbc.RA118.007222 PMID: 30814253

15. Zhuo XF, Wang J, Zhang J, Jiang LL, Hu HY, Lu JX. Solid-State NMR Reveals the Structural Transfor-mation of the TDP-43 Amyloidogenic Region upon Fibrillation. J Am Chem Soc. 2020. https://doi.org/10.1021/jacs.9b10736 PMID: 32003979

16. Gui X, Luo F, Li Y, Zhou H, Qin Z, Liu Z, et al. Structural basis for reversible amyloids of hnRNPA1 eluci-dates their role in stress granule assembly. Nat Commun. 2019; 10:2006. https://doi.org/10.1038/s41467-019-09902-7 PMID: 31043593

17. Molliex A, Temirov J, Lee J, Coughlin M, Kanagaraj AP, Kim HJ, et al. Phase separation by low com-plexity domains promotes stress granule assembly and drives pathological fibrillization. Cell. 2015; 163:123–133. https://doi.org/10.1016/j.cell.2015.09.015 PMID: 26406374

18. Patel A, Lee HO, Jawerth L, Maharana S, Jahnel M, Hein MY, et al. A Liquid-to-Solid Phase Transition of the ALS Protein FUS Accelerated by Disease Mutation. Cell. 2015; 162:1066–1077. https://doi.org/10.1016/j.cell.2015.07.047 PMID: 26317470

19. Cao Q, Boyer DR, Sawaya MR, Ge P, Eisenberg DS. Cryo-EM structures of four polymorphic TDP-43 amyloid cores. Nat Struct Mol Biol. 2019; 26:619–627. https://doi.org/10.1038/s41594-019-0248-4 PMID: 31235914

20. Barbieri EM, Shorter J. TDP-43 shapeshifts to encipher FTD severity. Nat Neurosci. 2019; 22:3–5. https://doi.org/10.1038/s41593-018-0299-6 PMID: 30559481

21. Laferrière F, Maniecka Z, Pérez-Berlanga M, Hruska-Plochan M, Gilhespy L, Hock EM, et al. TDP-43 extracted from frontotemporal lobar degeneration subject brains displays distinct aggregate assemblies and neurotoxic effects reflecting disease progression rates. Nat Neurosci. 2019; 22:65–77. https://doi.org/10.1038/s41593-018-0294-y PMID: 30559480

22. Kroschwald S, Alberti S. Gel or Die: Phase Separation as a Survival Strategy. Cell. 2017; 168:947–948. https://doi.org/10.1016/j.cell.2017.02.029 PMID: 28283065

23. Riback JA, Katanski CD, Kear-Scott JL, Pilipenko EV, Rojek AE, Sosnick TR, et al. Stress-Triggered Phase Separation Is an Adaptive, Evolutionarily Tuned Response. Cell. 2017; 168:1028–1040.e1019. https://doi.org/10.1016/j.cell.2017.02.027 PMID: 28283059

24. van Leeuwen W, Rabouille C. Cellular stress leads to the formation of membraneless stress assemblies in eukaryotic cells. Traffic. 2019; 20:623–638. https://doi.org/10.1111/tra.12669 PMID: 31152627

25. Asakawa K, Handa H, Kawakami K. Optogenetic modulation of TDP-43 oligomerization accelerates ALS-related pathologies in the spinal motor neurons. Nat Commun. 2020; 11:1004. https://doi.org/10.1038/s41467-020-14815-x PMID: 32081878

26. Pantoja-Uceda D, Stuani C, Laurents DV, McDermott AE, Buratti E, Mompeán M NMR assignments for the C-terminal domain of human TDP-43. Biomol NMR Assign. 2021. https://doi.org/10.1007/s12104-020-10002-7 Epub ahead of print. PMID: 33417141

27. Settembre C, Fraldi A, Medina DL, Ballabio A. Signals from the lysosome: a control centre for cellular clearance and energy metabolism. Nat Rev Mol Cell Biol. 2013; 14:283–296. https://doi.org/10.1038/nrm3565 PMID: 23609508

28. Martin EW, Holehouse AS, Peran I, Farag M, Incicco JJ, Bremer A, et al. Valence and patterning of aro-matic residues determine the phase behavior of prion-like domains. Science. 2020; 367:694–699. https://doi.org/10.1126/science.aaw8653 PMID: 32029630

29. Mompeán M, Li W, Li J, Laage S, Siemer AB, Bozkurt G, et al. The Structure of the Necrosome RIPK1-RIPK3 Core, a Human Hetero-Amyloid Signaling Complex. Cell. 2018; 173:1244–1253.e1210. https://doi.org/10.1016/j.cell.2018.03.032 PMID: 29681455

30. Murray DT, Kato M, Lin Y, Thurber KR, Hung I, McKnight SL, et al. Structure of FUS Protein Fibrils and Its Relevance to Self-Assembly and Phase Separation of Low-Complexity Domains. Cell. 2017; 171:615–627 e616. https://doi.org/10.1016/j.cell.2017.08.048 PMID: 28942918

31. Qiuye L, Babinchak W, Surewicz WK. Cryo-EM structure of amyloid fibrils formed by the entire low complexity domain of TDP-43. bioRxiv. 2020.12.14.422689v1 [Preprint]. 2020 [cited 2020 Dec 15]. https://doi.org/10.1101/2020.12.14.422689

32. Jiang LL, Che MX, Zhao J, Zhou CJ, Xie MY, Li HY, et al. Structural transformation of the amyloidogenic core region of TDP-43 protein initiates its aggregation and cytoplasmic inclusion. J Biol Chem. 2013; 288:19614–19624. https://doi.org/10.1074/jbc.M113.463828 PMID: 23689371

33. Shenoy J, El Mammeri N, Dutour A, Berbon M, Saad A, Lends A, et al. Structural dissection of amyloid aggregates of TDP-43 and its C-terminal fragments TDP-35 and TDP-16. FEBS J. 2019. https://doi.org/10.1111/febs.15159 PMID: 31782904

34. Lu JX, Qiang W, Yau WM, Schwieters CD, Meredith SC, Tycko R. Molecular structure of beta-amyloid fibrils in Alzheimer's disease brain tissue. Cell. 2013; 154:1257–1268. https://doi.org/10.1016/j.cell.2013.08.035 PMID: 24034249

35. Qiang W, Yau WM, Lu JX, Collinge J, Tycko R. Structural variation in amyloid-beta fibrils from Alzheimer's disease clinical subtypes. Nature. 2017; 541:217–221. https://doi.org/10.1038/nature20814 PMID: 28052060

36. Wälti MA, Ravotti F, Arai H, Glabe CG, Wall JS, Böckmann A, et al. Atomic-resolution structure of a disease-relevant Abeta(1–42) amyloid fibril. Proc Natl Acad Sci U S A. 2016; 113:E4976–4984. https://doi.org/10.1073/pnas.1600749113 PMID: 27469165

37. Gasset-Rosa F, Lu S, Yu H, Chen C, Melamed Z, Guo L, et al. Cytoplasmic TDP-43 De-mixing Independent of Stress Granules Drives Inhibition of Nuclear Import, Loss of Nuclear TDP-43, and Cell Death. Neuron. 2019; 102:339–357.e337. https://doi.org/10.1016/j.neuron.2019.02.038 PMID: 30853299

38. Chou CC, Zhang Y, Umoh ME, Vaughan SW, Lorenzini I, Liu F, et al. TDP-43 pathology disrupts nuclear pore complexes and nucleocytoplasmic transport in ALS/FTD. Nat Neurosci. 2018; 21:228–239. https://doi.org/10.1038/s41593-017-0047-3 PMID: 29311743

39. Li N, Lagier-Tourenne C. Nuclear pores: the gate to neurodegeneration. Nat Neurosci. 2018; 21:156–158. https://doi.org/10.1038/s41593-017-0066-0 PMID: 29371653

40. Kjaergaard M, Brander S, Poulsen FM. Random coil chemical shift for intrinsically disordered proteins: effects of temperature and pH. J Biomol NMR. 2011; 49:139–149. https://doi.org/10.1007/s10858-011-9472-x PMID: 21234644

41. Kjaergaard M, Poulsen FM. Sequence correction of random coil chemical shifts: correlation between neighbor correction factors and changes in the Ramachandran distribution. J Biomol NMR. 2011; 50:157–165. https://doi.org/10.1007/s10858-011-9508-2 PMID: 21604143

42. Schwarzinger S, Kroon GJ, Foss TR, Chung J, Wright PE, Dyson HJ. Sequence-dependent correction of random coil NMR chemical shifts. J Am Chem Soc. 2001; 123:2970–2978. https://doi.org/10.1021/ja003760i PMID: 11457007

43. Delaglio F, Grzesiek S, Vuister GW, Zhu G, Pfeifer J, Bax A. NMRPipe: a multidimensional spectral processing system based on UNIX pipes. J Biomol NMR. 1995; 6:277–293. https://doi.org/10.1007/BF00197809 PMID: 8520220

44. Lee W, Tonelli M, Markley JL. NMRFAM-SPARKY: enhanced software for biomolecular NMR spectroscopy. Bioinformatics. 2015; 31:1325–1327. https://doi.org/10.1093/bioinformatics/btu830 PMID: 25505092

45. Takegoshi K, Nakamura S, Terao T. 13C–1H dipolar-assisted rotational resonance in magic-angle spinning NMR. Chem Phys Lett. 2001 344:631–637. https://doi.org/10.1016/S0009-2614(01)00791-6

46. Heyduk T, Ma Y, Tang H, Ebright RH. Fluorescence anisotropy: rapid, quantitative assay for protein-DNA and protein-protein interaction. Methods Enzymol. 1996; 274:492–503. https://doi.org/10.1016/s0076-6879(96)74039-9 PMID: 8902827